# Experimental Investigation of the Effect of Piezoelectric Sensor Position on Signal Characteristics and Classification via Machine Learning

Nihat Çankaya
Department of Electronics and Automation, Control and Automation Technology
Konya Organized Industrial Zone Vocational School, Necmettin Erbakan University
Konya, Turkey
ncankaya@erbakan.edu.tr

***Abstract*—In this study, the signals generated by steel balls dropped onto a plate were experimentally investigated with respect to the position of the piezoelectric sensor attached to the plate, and these signals were automatically classified using machine learning methods. When the sensor was mounted on the bottom surface, the mean RMS value was measured as $1.07 \pm 0.03$ V, kurtosis as $17.42 \pm 1.49$, and crest factor as $4.83 \pm 0.13$; in the side-edge configuration, the RMS dropped to $0.72 \pm 0.03$ V while kurtosis rose to $31.12 \pm 3.08$ and crest factor to $7.21 \pm 0.29$. In the frequency domain, the bottom configuration concentrated its energy in a relatively narrow band with a centroid frequency of $313.76 \pm 3.40$ kHz, bandwidth of $116.95 \pm 7.86$ kHz, and spectral kurtosis of $2.91 \pm 0.27$; the side configuration exhibited a richer, multimodal frequency content with a centroid of $339.89 \pm 23.26$ kHz and spectral kurtosis of $4.40 \pm 0.83$. Machine learning analyses were conducted at three levels: (1) separate classification of five time-domain and five frequency-domain features using five algorithms, (2) minimum-feature analysis, and (3) noise robustness analysis. SVM, Random Forest, KNN, Logistic Regression, and Naive Bayes all achieved 100% classification accuracy with both feature sets. In the minimum-feature analysis, RMS (Cohen's $d = 13.08$) was identified as the single most discriminative feature, achieving 100% accuracy alone. In the noise robustness test, time-domain features maintained 100% accuracy down to $-5$ dB SNR, while frequency-domain features degraded to 98.6% under the same condition. These results demonstrate that sensor placement is a critical design parameter that directly determines detection sensitivity and signal interpretation in piezoelectric-based impact monitoring systems.**

***Index Terms*—Piezoelectric sensor, impact detection, sensor position, time/frequency-domain features, machine learning, structural health monitoring.**

## I. Introduction

Foreign object impacts on plate and shell structures pose a significant threat to structural integrity in fields such as aerospace, marine, and automotive engineering; timely detection, localization, and damage assessment of impact damage are primary objectives of structural health monitoring (SHM) systems.

In this paper, the impact signals generated by steel balls dropped onto a plate are experimentally recorded in two configurations—with the piezoelectric sensor mounted on the bottom surface or on the side edge of the plate—compared using time- and frequency-domain features commonly employed in the literature, and automatically classified using machine learning methods.

Low-velocity impact events can be modeled within the framework of classical Hertzian contact theory [1]–[3]. The resulting mechanical strain changes are converted to voltage signals by piezoelectric (PZT) sensors mounted on the structure [4]–[6]. Arrival-time differences from multi-sensor arrays serve as the primary source for impact localization [7]–[9]. Modal decomposition of acoustic emission signals and damage classification have also been extensively studied [10]–[15]. Lamb-wave-based SHM studies focus on sensor array optimization [16]–[19], yet the effect of an individual sensor's mounting surface on signal characteristics has not been addressed separately. While much of the literature on piezoelectric-sensor-based impact detection examines sensor array placement accuracy [20]–[22], how the mounting surface alters the signal's time/frequency-domain features has received relatively little attention. Machine learning and deep learning methods are attracting increasing interest in SHM [23]–[26], with various ML approaches successfully applied to impact localization and damage characterization [27], [28].

Section II presents the experimental setup and data acquisition system, Section III discusses signal analysis and machine learning results, and Section IV provides a general evaluation. Table I summarizes the main approaches addressed in the literature.

## II. Material and Method

### A. Experimental Setup

The experimental setup consists of a circular metal plate placed on a plastic base, a guide rod positioned perpendicular to the center of the plate, and a perforated 3D-printed holder at the top of the rod through which a steel ball can be dropped freely. The ball is released from the holder positioned 20 cm above the plate surface and strikes the center of the plate.

TABLE I. PRINCIPAL APPROACHES USED IN IMPACT DETECTION, LOCALIZATION, AND DAMAGE ASSESSMENT

| Approach | Fundamental Principle | Related Studies |
|---|---|---|
| Contact mechanics / Hertzian model | Analytical/experimental modeling of the impact force pulse and resulting stress waves | [1], [2], [3] |
| Piezoelectric force detection | Acquisition of the impact force signal via PZT sensors and interface circuits | [4], [5], [6] |
| Probability/error-index-based localization | Probabilistic/optimization-based evaluation of arrival-time differences from a sensor array | [7], [8], [9] |
| Sensor placement optimization | Physics-based and genetic-algorithm-driven optimal sensor positioning | [20], [21], [22] |
| Acoustic emission and modal decomposition | Classification of damage-induced emissions via wavenumber–frequency modal separation | [10], [11], [14], [15] |
| Lamb-wave-based SHM | Directed wave propagation and array-based multi-damage localization | [16], [17], [18], [19] |
| ML-based impact detection and classification | Location and damage estimation from signal features using conventional ML algorithms | [27], [28], [12], [13] |
| Deep learning for impact analysis | Impact recognition via RNN, self-attention, transfer learning, and multi-task DL | [23], [24], [25], [26] |

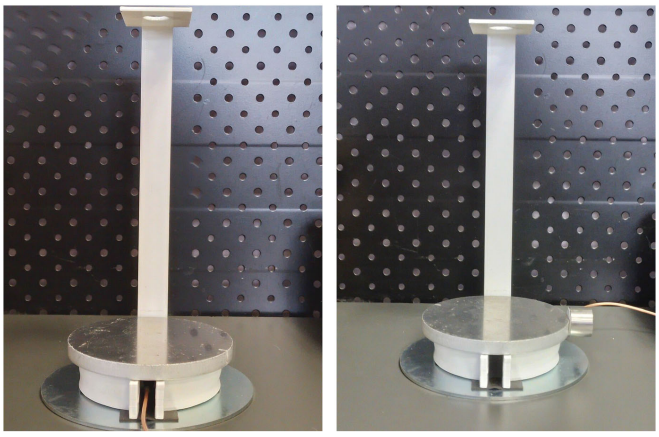



Fig. 1. General view of the experimental setup: (a) sensor mounted on the bottom surface of the plate, (b) sensor mounted on the side edge of the plate

The piezoelectric sensor (resonance frequency 150 kHz) was mounted either on the bottom surface or on the side edge of the plate, corresponding to the two main configurations of the study, as shown in Fig. 1.

### B. Data Acquisition System

The weak voltage signal from the piezoelectric sensor was first amplified by a preamplifier/filter unit at 40 dB gain (100×), then digitized at 1 MSPS using a USB-based digital oscilloscope and transferred to a computer. Fig. 2 shows a top view of the ball guide and plate together with the hardware components of the measurement system. The ball-drop experiment was repeated three times for each configuration, yielding a total of six recordings labeled `bottom_1–bottom_3` and `side_1–side_3`. Each recording is approximately 1.05 s in duration.

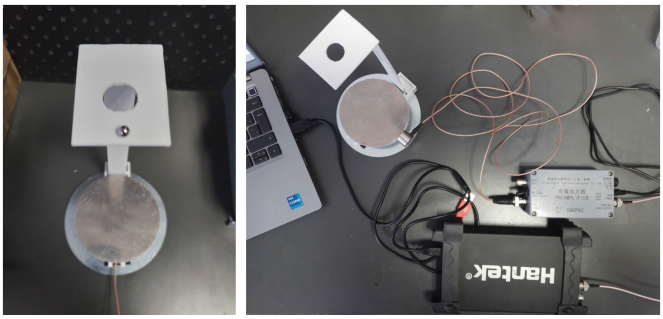



Fig. 2. (a) Top view of the region where the ball strikes the plate; (b) measurement system consisting of a computer, piezoelectric sensor, preamplifier, and USB oscilloscope

### C. Signal Processing and Feature Extraction

In each recording, the active window was defined as the region between the first and last samples at which the signal envelope $|x(t)|$ exceeded a fixed fraction of the maximum amplitude, with a short margin added to encompass the decay tail. This procedure yielded active windows averaging 73 ms for the bottom configuration and 64 ms for the side configuration.

Over each active window, five time-domain and five frequency-domain features most commonly used in the impact/acoustic-emission characterization literature were computed. Feature definitions are given in Table II and Table III. Frequency-domain features were computed from the power spectrum $P(f)$ obtained via the FFT of the Hanning-windowed signal, normalized to total energy.

## III. RESULTS AND DISCUSSION

### A. Active Impact Windows

Fig. 3 shows the active windows of both configurations in close-up view. In both signals, secondary impacts (bounces) following the main strike with decreasing amplitude are clearly

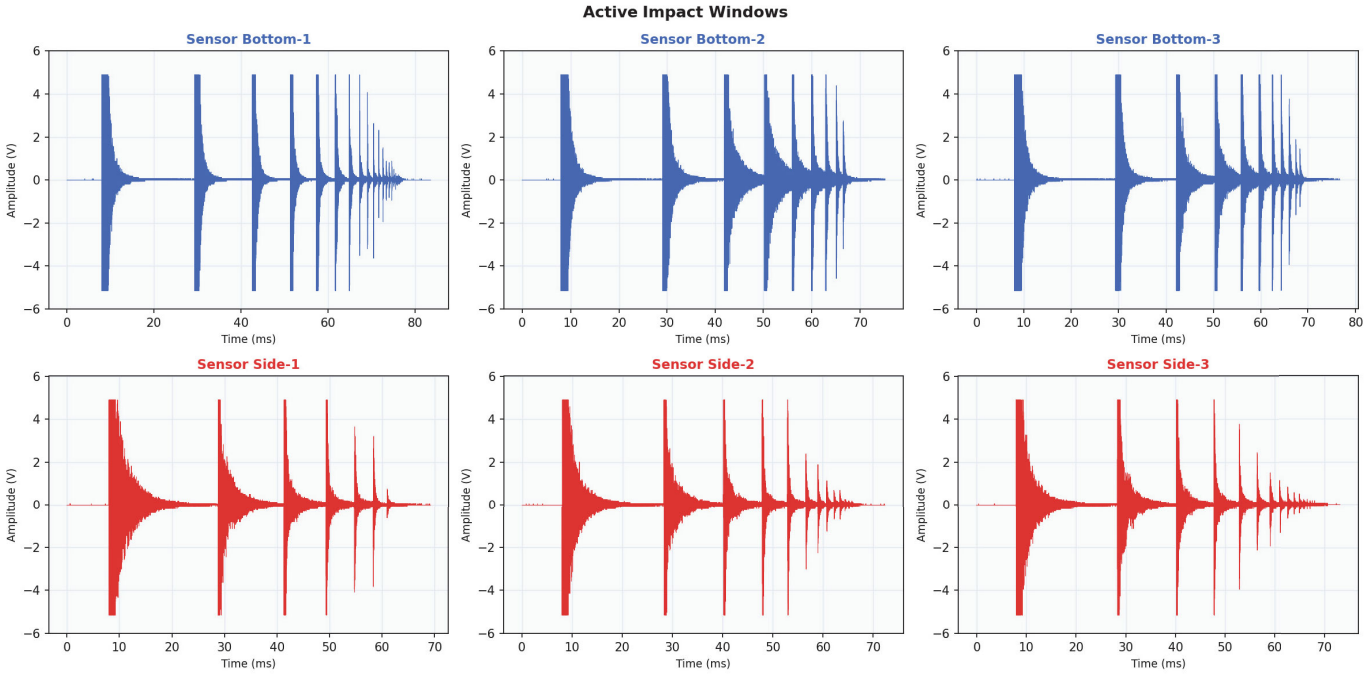



Fig. 3. Active impact windows. Top row: bottom configuration; bottom row: side configuration

TABLE II. DEFINITIONS OF THE COMPUTED TIME-DOMAIN FEATURES

| Feature | Formula | Description |
|---|---|---|
| RMS | $\sqrt{\frac{1}{N}\sum_{i=1}^{N} x_i^2}$ | Average energy level |
| Kurtosis | $\frac{\frac{1}{N}\sum(x_i-\mu)^4}{\sigma^4}$ | Impulsiveness measure |
| Crest Factor | $Peak/RMS$ | Degree of impulsiveness |
| Skewness | $\frac{\frac{1}{N}\sum(x_i-\mu)^3}{\sigma^3}$ | Distribution asymmetry |
| ZCR | $\frac{1}{N}\sum\lvert\mathrm{sgn}(x_{i+1})-\mathrm{sgn}(x_i)\rvert$ | Zero-crossing rate |

TABLE III. DEFINITIONS OF THE COMPUTED FREQUENCY-DOMAIN FEATURES

| Feature | Formula | Description |
|---|---|---|
| Centroid Freq. | $f_c = \frac{\sum f\cdot P(f)}{\sum P(f)}$ | Spectral energy center |
| RMS Frequency | $\sqrt{\frac{\sum f^2 P(f)}{\sum P(f)}}$ | Effective frequency location |
| Bandwidth | $\sqrt{\sum(f-f_c)^2 P(f)}$ | Spectral spread |
| Spectral Kurtosis | $\frac{\sum(f-f_c)^4 P(f)}{\sigma_f^4}$ | Spectral peakedness |
| Spectral Entropy | $-\sum P_n \log_2 P_n$ | Spectral irregularity |

visible. Damping occurs more rapidly in the side configuration and the recording duration is shorter.

### B. Frequency-Domain Analysis

Fig. 4 shows the mean FFT spectrum and min–max range over three repetitions for both configurations. The bottom configuration spectrum is characterized by a relatively small number of distinct dominant frequency components (approximately 26, 244, and 394 kHz); the side configuration exhibits a rich, multimodal structure spread across the 0–500 kHz band.

Spectrograms of recordings Bottom-1 and Side-1 are presented in Fig. 5. In the bottom configuration energy concentrates in a few narrow frequency bands, whereas in the side configuration a rich content spread across the entire frequency band is observed.

TABLE IV. PER-RECORDING TIME-DOMAIN FEATURE VALUES

| Record | RMS (V) | Peak (V) | P2P (V) | Kurt. | CF |
|---|---|---|---|---|---|
| Bottom-1 | 1.05 | 5.15 | 10.04 | 18.89 | 4.93 |
| Bottom-2 | 1.10 | 5.15 | 10.04 | 15.92 | 4.68 |
| Bottom-3 | 1.06 | 5.15 | 10.04 | 17.45 | 4.87 |
| Side-1 | 0.75 | 5.15 | 10.04 | 27.70 | 6.91 |
| Side-2 | 0.71 | 5.15 | 10.04 | 31.98 | 7.24 |
| Side-3 | 0.69 | 5.15 | 10.04 | 33.68 | 7.48 |

### C. Time- and Frequency-Domain Feature Values

Per-recording feature values are given in Table IV and Table V; group means are summarized in Table VI.

The RMS value in the bottom configuration (1.07 V) is higher than that of the side configuration (0.72 V). Kurtosis and crest factor are lower in the bottom configuration (17.42 and 4.83) than in the side (31.12 and 7.21), reflecting a more energetic, less impulsive response due to the sensor's direct coupling to the impact point. In the side configuration, higher kurtosis/crest factor indicate a spikier signal character, while

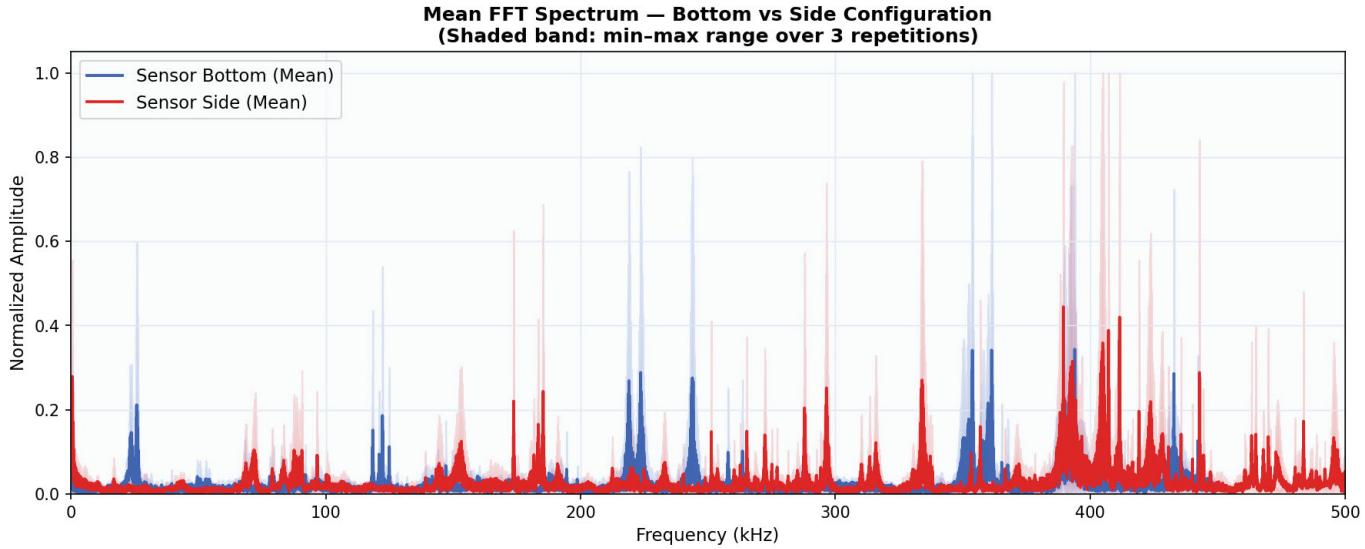



Fig. 4. Mean FFT spectrum for Bottom and Side configurations. The shaded band indicates the min–max range over three repetitions

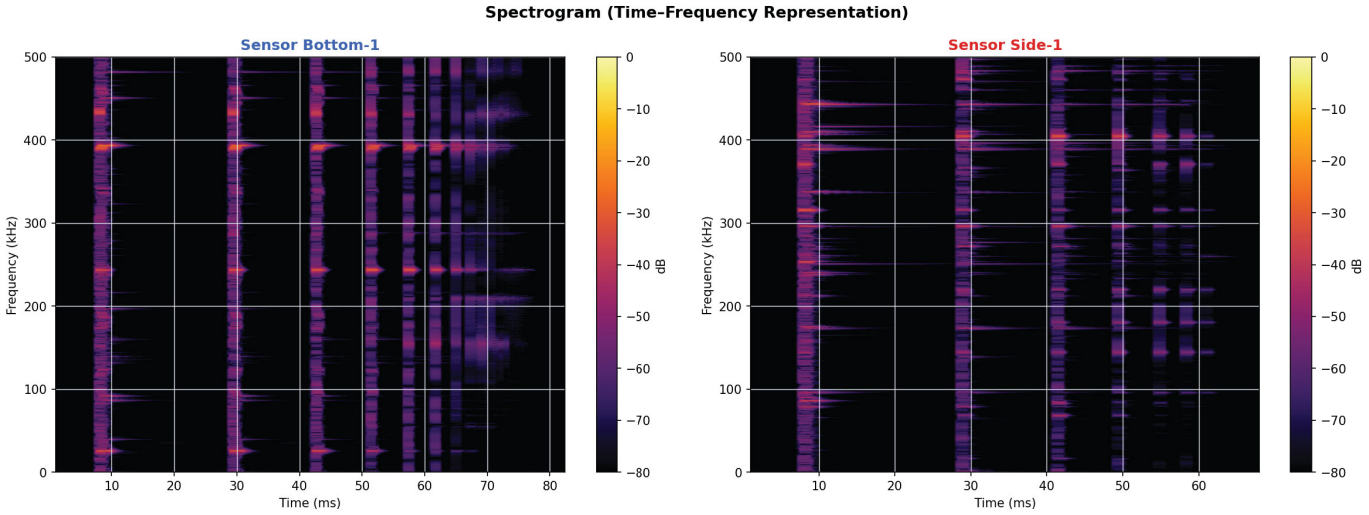



Fig. 5. Spectrogram (STFT). Left: Sensor Bottom-1; Right: Sensor Side-1

TABLE V. PER-RECORDING FREQUENCY-DOMAIN FEATURE VALUES

| Record | Peak f. (kHz) | Centroid (kHz) | RMS f. (kHz) | Sp.K. | BW (kHz) |
|---|---|---|---|---|---|
| Bottom-1 | 394.00 | 312.10 | 335.90 | 3.17 | 124.10 |
| Bottom-2 | 243.90 | 317.70 | 339.00 | 2.63 | 118.30 |
| Bottom-3 | 393.90 | 311.50 | 329.80 | 2.92 | 108.50 |
| Side-1 | 405.30 | 348.60 | 366.50 | 4.68 | 113.20 |
| Side-2 | 389.60 | 357.50 | 373.30 | 5.04 | 107.30 |
| Side-3 | 389.70 | 313.50 | 335.10 | 3.46 | 118.40 |

TABLE VI. GROUP MEANS OF TIME- AND FREQUENCY-DOMAIN FEATURES (MEAN± STD. DEV., $n = 3$)

| Feature | Sensor Bottom | Sensor Side |
|---|---|---|
| RMS (V) | $1.07 \pm 0.03$ | $0.72 \pm 0.03$ |
| Kurtosis | $17.42 \pm 1.49$ | $31.12 \pm 3.08$ |
| Crest Factor | $4.83 \pm 0.13$ | $7.21 \pm 0.29$ |
| Centroid Freq. (kHz) | $313.76 \pm 3.40$ | $339.89 \pm 23.26$ |
| RMS Frequency (kHz) | $334.89 \pm 4.64$ | $358.32 \pm 20.36$ |
| Bandwidth (kHz) | $116.95 \pm 7.86$ | $112.96 \pm 5.56$ |
| Spectral Kurtosis | $2.91 \pm 0.27$ | $4.40 \pm 0.83$ |

the lower RMS points to additional attenuation losses from wave propagation.

In the frequency domain, the spectral kurtosis of the side configuration (4.40) exceeds that of the bottom (2.91), suggesting that the sensor captures more Lamb-wave modes prop-

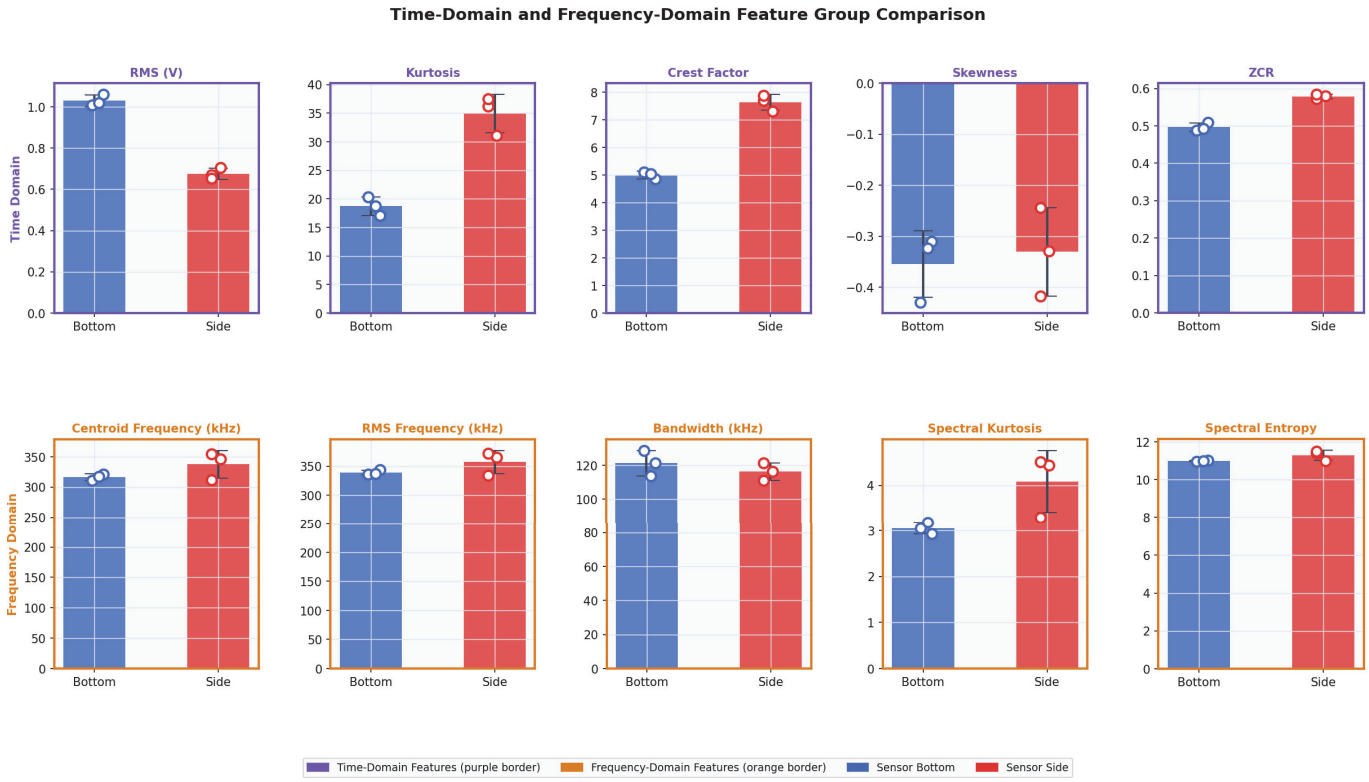



Fig. 6. Group comparison of time-domain (top row, purple border) and frequency-domain (bottom row, orange border) features. Error bars indicate $n = 3$ standard deviation

agating across the plate, yielding richer multimodal content consistent with the wave dispersion literature [16]–[19].

## IV. Machine Learning Classification

In this section, the computed time- and frequency-domain features are used to automatically classify the sensor mounting position (Bottom/Side) via machine learning. Similar approaches have been successfully applied to impact localization [27] and damage characterization [28]. All analyses employ five algorithms: Support Vector Machine (SVM — linear kernel), Random Forest (200 trees), K-Nearest Neighbors (KNN, $k = 1$), Logistic Regression, and Naive Bayes. The Peak and P2P features were excluded because they remained constant at the saturation limit of the measurement device (5.15 V and 10.04 V).

### A. Analysis 1: Time- and Frequency-Domain Classification

Five time-domain features (RMS, Kurtosis, Crest Factor, Skewness, ZCR) and five frequency-domain features (Centroid Frequency, RMS Frequency, Bandwidth, Spectral Kurtosis, Spectral Entropy) were presented to the algorithms separately, and classification accuracy was evaluated independently for each domain.

Fig. 6 shows the group comparison of both feature sets between Bottom and Side, and Fig. 7 shows the confusion matrices.

As shown in Table VII, all five algorithms achieved 100% classification accuracy with both feature sets. This result demonstrates that sensor mounting position leaves distinct, automatically distinguishable traces in both the time and frequency domains.

TABLE VII. Analysis 1: Classification Accuracy for Time- and Frequency-Domain Features

| Algorithm | Time Domain | Frequency Domain |
|---|---|---|
| SVM | 100% | 100% |
| Random Forest | 100% | 100% |
| KNN | 100% | 100% |
| Logistic Regression | 100% | 100% |
| Naive Bayes | 100% | 100% |

### B. Analysis 2: Minimum-Feature Analysis

Each feature was individually supplied to five algorithms; the mean classification accuracy and Cohen's $d$ effect size were computed. The goal is to identify which single feature is sufficient for the simplest possible implementation of the system.

As shown in Fig. 8 and Table VIII, four time-domain features (RMS, Crest Factor, ZCR, Kurtosis) individually achieve 100% classification accuracy, whereas all frequency-domain features individually remain in the 70–90% range. The strongest single feature is RMS with Cohen's $d = 13.08$.

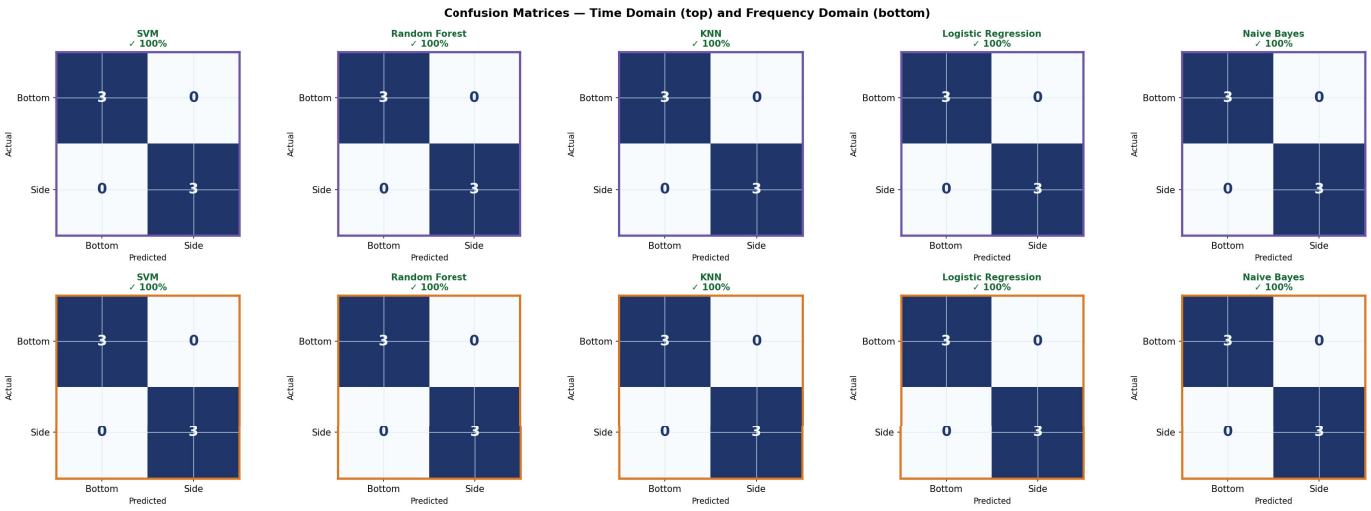



Fig. 7. Confusion matrices. Top row: time domain; bottom row: frequency domain

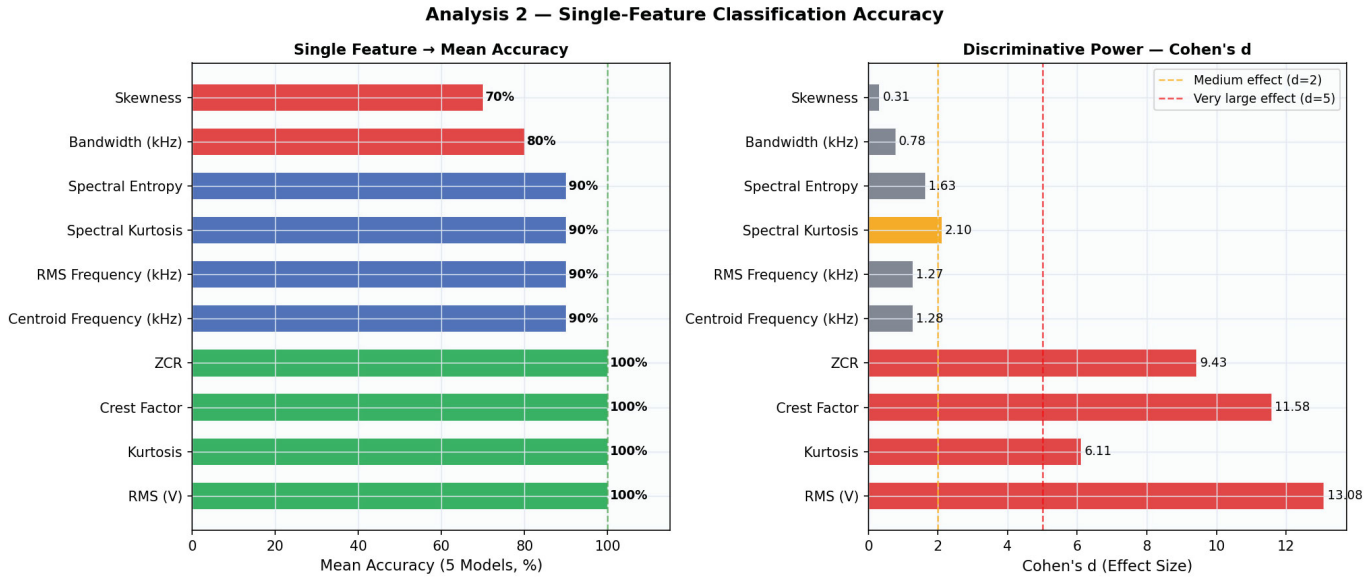



Fig. 8. Mean classification accuracy with a single feature (left) and Cohen's $d$ effect size (right)

This finding has practical implications: in real-time or computationally constrained systems, computing only the RMS is sufficient.

### C. Analysis 3: Noise Robustness

White Gaussian noise was added to the raw signals at seven SNR levels (30, 20, 15, 10, 5, 0, and $-5$ dB), and 30 Monte Carlo trials were performed at each level. Classification accuracies of the time- and frequency-domain feature sets were evaluated separately under noise.

As shown in Fig. 9 and Table IX, time-domain features maintained 100% accuracy across all SNR levels, while frequency-domain features degraded to 98.6% only at $-5$ dB. This demonstrates that time-domain features are markedly more robust to noise than frequency-domain features. In real field conditions with high environmental noise, time-domain features are recommended.

## V. Conclusion

In this paper, the characteristics of impact signals generated by steel balls dropped onto a plate were experimentally investigated as a function of piezoelectric sensor mounting position, and the signals were automatically classified using machine learning. The key findings are as follows:

The bottom configuration exhibited a more energetic response with higher RMS (1.07 V) and lower kurtosis/crest factor; the side configuration showed lower RMS (0.72 V), higher kurtosis/crest factor, and richer multimodal frequency content.

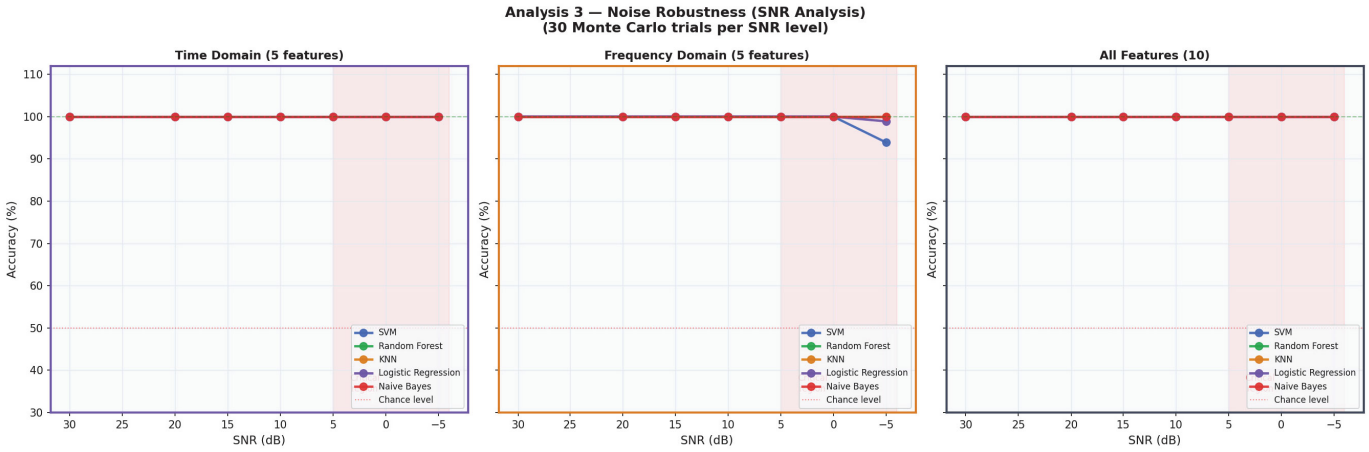



Fig. 9. Noise robustness analysis. Left: time domain; center: frequency domain; right: all features. Each point is the mean of 30 Monte Carlo trials

TABLE VIII. ANALYSIS 2: SINGLE-FEATURE CLASSIFICATION ACCURACY AND COHEN'S $d$

| Feature | Dom. | Mean Acc. | Cohen's $d$ |
|---|---|---|---|
| RMS | Time | 100% | 13.08 |
| Crest Factor | Time | 100% | 11.58 |
| ZCR | Time | 100% | 9.43 |
| Kurtosis | Time | 100% | 6.11 |
| Spectral Kurtosis | Freq. | 90% | 2.10 |
| Centroid Freq. | Freq. | 90% | 1.28 |
| Spectral Entropy | Freq. | 90% | 1.63 |
| RMS Frequency | Freq. | 90% | 1.27 |
| Bandwidth | Freq. | 80% | 0.78 |
| Skewness | Time | 70% | 0.31 |

TABLE IX. ANALYSIS 3: MEAN CLASSIFICATION ACCURACY (%) VS. SNR (5-ALGORITHM MEAN, 30 TRIALS)

| SNR (dB) | Time | Frequency | All (10) |
|---|---|---|---|
| 30 | 100.0 | 100.0 | 100.0 |
| 20 | 100.0 | 100.0 | 100.0 |
| 15 | 100.0 | 100.0 | 100.0 |
| 10 | 100.0 | 100.0 | 100.0 |
| 5 | 100.0 | 100.0 | 100.0 |
| 0 | 100.0 | 100.0 | 100.0 |
| $-5$ | 100.0 | 98.6 | 100.0 |

In the machine learning analyses: (1) When five time-domain and five frequency-domain features were independently evaluated with five algorithms, 100% classification accuracy was achieved with both feature sets. (2) In the minimum-feature analysis, RMS was identified as the strongest single feature (Cohen's $d = 13.08$) capable of achieving 100% accuracy alone. (3) In the noise robustness analysis, time-domain features maintained 100% accuracy down to $-5$ dB SNR, while frequency-domain features degraded to 98.6% under the same condition.

These findings demonstrate that sensor placement is a critical design parameter not only for localization accuracy but also for statistical/spectral signal interpretation and machine-learning-based automatic recognition in piezoelectric-based impact monitoring systems. A limitation of this study is the amplitude saturation observed during the main impact pulse; future work should address reduced amplifier gain, increased repetition count, testing of different sensor angles and materials, and application of statistical significance tests.

## ACKNOWLEDGMENT

The author thanks Muhammet Emre Irmak for his contributions to this study.

## REFERENCES

[1] G. Mclaskey and S. Glaser, "Hertzian impact: experimental study of the force pulse and resulting stress waves," *J. Acoust. Soc. Am.*, vol. 128, no. 3, pp. 1087–1096, 2010, doi: 10.1121/1.3466847.

[2] Q. Peng, X. Liu, and Y. Wei, "Elastic impact of sphere on large plate," *J. Mech. Phys. Solids*, vol. 156, art. 104604, 2021, doi: 10.1016/j.jmps.2021.104604.

[3] C. D. Garcia-Mendoza and N. Sablón Cossío, "Contact Mechanics for a Ball Dropped on an Infinite Plate, an Update," in *1st Australian IEOM Conf.*, Sydney, 2022, doi: 10.46254/au01.20220580.

[4] J. Liu *et al.*, "A Study on Impact Force Detection Method Based on Piezoelectric Sensing," *Sensors*, vol. 22, no. 14, art. 5167, 2022, doi: 10.3390/s22145167.

[5] L. Capineri and A. Bulletti, "A Versatile Analog Electronic Interface for Piezoelectric Sensors Used for Impacts Detection and Positioning in SHM Systems," *Electronics*, vol. 10, art. 1047, 2021, doi: 10.3390/electronics10091047.

[6] X. Huang *et al.*, "Impact Monitoring and Positioning Method of Steel Plate Based on Piezoelectric Acoustic Sensor Array," in *SPAWDA*, 2023, doi: 10.1109/spawda60286.2023.10412327.

[7] R. Gorgin *et al.*, "Probability based impact localization in plate structures using an error index," *Mech. Syst. Signal Process.*, vol. 157, art. 107724, 2021, doi: 10.1016/j.ymssp.2021.107724.

[8] S. Sikdar, P. Mirgal, and S. Banerjee, "Low-velocity Impact Source Localization in a Composite Sandwich Structure using a Broadband Piezoelectric Sensor Network," *Compos. Struct.*, 2022, doi: 10.1016/j.compstruct.2022.115619.

[9] I. Katsidimas *et al.*, "An Impact Localization Solution Using Embedded Intelligence via a Resource-Constrained IoT Device," *Sensors*, vol. 23, no. 2, art. 896, 2023, doi: 10.3390/s23020896.

[10] N. Rajic *et al.*, "In situ wavenumber–frequency modal decomposition of acoustic emissions," *Struct. Health Monit.*, vol. 19, no. 6, pp. 2033–2050, 2020, doi: 10.1177/1475921719885324.

[11] J. Gray, "In-situ modal decomposition of acoustic emission events arising from low-velocity impacts," *Mater. Res. Proc.*, 2025, doi: 10.21741/9781644903513-15.

[12] H. Altammar *et al.*, "Integrating Sensors in 3D Printed Structures for Impact Identification," in *ICCED*, 2024, doi: 10.1109/icced64257.2024.10983625.

[13] B. Uprety *et al.*, "A comparative evaluation of piezoelectric sensors for acoustic emission-based impact location estimation," *AIP Conf. Proc.*, vol. 1650, pp. 1146–1154, 2015, doi: 10.1063/1.4914724.

[14] R. James, R. Joseph, and V. Giurgiutiu, "Impact Damage Ascertainment in Composite Plates Using In-Situ Acoustic Emission Signal Signature Identification," *J. Compos. Sci.*, vol. 5, no. 3, art. 79, 2021, doi: 10.3390/jcs5030079.

[15] S. W. Kim *et al.*, "Acoustic emission based damage characterization in composite plates using low-velocity impact testing," *SHM*, 2015, doi: 10.12783/shm2015/185.

[16] K. Diamanti, J. Hodgkinson, and C. Soutis, "Detection of Low-velocity Impact Damage in Composite Plates using Lamb Waves," *Struct. Health Monit.*, vol. 3, no. 1, pp. 33–41, 2004, doi: 10.1177/1475921704041869.

[17] M. Philibert *et al.*, "Direct-write piezoelectric coating transducers in combination with discrete ceramic transducer for ultrasonic impact damage detection," *Struct. Health Monit.*, vol. 21, no. 4, pp. 1645–1660, 2021, doi: 10.1177/14759217211040719.

[18] C.-D. Chen *et al.*, "A Lamb-wave based SHM for multi-damage localizations in large composite plates," *Smart Mater. Struct.*, vol. 33, 2024, doi: 10.1088/1361-665x/ad3160.

[19] C. Liu *et al.*, "Analysis of Lamb wave propagation in a functionally graded piezoelectric small-scale plate," *Compos. Struct.*, 2021, doi: 10.1016/j.compstruct.2021.113733.

[20] Z. Ismail *et al.*, "Physics-based artificial neural network model for sensor placement optimization towards structural health monitoring," *Proc. SPIE*, 2025, doi: 10.1117/12.3051377.

[21] Y. Tan and L. Zhang, "Computational methodologies for optimal sensor placement in structural health monitoring: A review," *Struct. Health Monit.*, vol. 19, no. 5, pp. 1380–1408, 2020, doi: 10.1177/1475921719877579.

[22] R. Soman and P. Malinowski, "A Real-Valued Genetic Algorithm for Optimization of Sensor Placement for Guided Wave-Based Structural Health Monitoring," *Shock Vib.*, 2019, doi: 10.1155/2019/9614630.

[23] A. Humer *et al.*, "Localization of Impacts on Thin-Walled Structures by Recurrent Neural Networks," *arXiv*, 2025, doi: 10.48550/arxiv.2505.08362.

[24] S. Karmakov and M. Aliabadi, "Deep Learning Approach to Impact Classification using Self-Attention," *Sensors*, vol. 22, no. 12, art. 4370, 2022, doi: 10.3390/s22124370.

[25] M. H. Yazdani *et al.*, "A Hybrid Deep Transfer Learning Framework for Delamination Identification," *Sensors*, vol. 25, no. 3, art. 826, 2025, doi: 10.3390/s25030826.

[26] H. Wang *et al.*, "Composite material impact damage monitoring based on multi-task deep learning," *Proc. SPIE*, 2026, doi: 10.1117/12.3093495.

[27] "Structural Health Monitoring for impact localisation via machine learning," *Mech. Syst. Signal Process.*, 2022, doi: 10.1016/j.ymssp.2022.109621.

[28] "Machine learning techniques for impact characterization and vibration based damage detection," *Technical Report*, Imperial College London, 2024, doi: 10.25560/109958.